ULTRASONIC IMAGING 4, 234-266 (1982)

MULTIPATH ARTIFACT CORRECTIONS IN ULTRASONIC TRANSMISSION TOMOGRAPHY[1]

C. R. Crawford and A. C. Kak

School of Electrical Engineering
Purdue University
W. Lafayette, IN 47907

This paper deals with computed imaging techniques for ultrasonic transmission tomography. Cross-sectional images of the refractive index in soft biological tissues can be obtained by measuring the arrival-time of signals that propagate between two transducers. An alternative method to obtain images is to measure the attenuation in the path between the pair of transducers. In practice, images of the refractive index exhibit a better quality than images of the attenuation coefficient. In this report we have shown through computer simulation that some of the degradations in images of the attenuation coefficient are due to the existence of multiple rays that link the transmitting and the receiving transducers. This condition is known as multipath. We have demonstrated two methods to reduce the influence of multipath on reconstructions of the attenuation coefficient. The first method employs homomorphic signal processing to estimate the attenuation coefficient for one of the linking rays. The second method applies median filtering in the projection space to remove the artifacts caused by multipath. The correction techniques were tested on data obtained by scanning tissue equivalent phantoms. Results obtained indicate that the correction methods significantly improve the quality of images of the attenuation coefficient.

Key words: Homomorphic filtering; median filtering; multipath artifacts; tomography; ultrasound.

1. INTRODUCTION

The introduction of X-ray computed tomography (CT) in 1972 brought forth a revolution in diagnostic medical imaging [1]. This powerful technique cannot be applied without first considering the possible health hazards of X-rays. For some medical applications, such as mass screening of the female breast, X-ray imaging is precluded as a viable diagnostic modality because it is invasive [2]. The need exists for techniques similar to CT, but with other forms of energy that are not invasive.

Ultrasound is an attractive substitute for X-rays because, at diagnostic power levels, it is thought to be harmless. Ultrasound offers the possibility for the characterization of the morphological state of a biological specimen by generating maps of acoustic parameters of the object. The two parameters of greatest interest are the attenuation coefficient and the refractive index.

The first attenuation images were reported by Greenleaf *et al.* [3] in 1974. The parameter they used for tomographic reconstructions was based on the total energy in the received waveform. This parameter is the direct analogy to the attenuation coefficient used in CT. The measurement in the ultrasound case is subject to error because the loss due to the specular reflection coefficient is ignored. As a result, the images produced by this technique are, at best, only qualitatively correct and often may be corrupted by artifacts.

[1]This work was supported by NIH grants GM24687 and GM2499403.

0161-7346/82/030234-33$02.00/0

Techniques to find quantitative estimates of the attenuation coefficient were shown by Kak and Dines [4]. These were derived as a consequence of the frequency dependence of the attenuation coefficient. Reconstructions based on these methods were shown elsewhere by Dines and Kak [5]. Quantitative results were reported by Klepper *et al.* [6].

The first quantitative refractive index ultrasonic tomograms were reported by Greenleaf *et al.* [7] in 1975. The parameter used for their technique was the transit time of the ultrasound waveform that travels from the transmitting transducer to the receiving transducer. This method is known as time-of-flight tomography. Tomograms made from the transit time are linearly related to the refractive index of the object. Carson *et al.* [8], Jakowatz and Kak [9], and Grover and Sharp [10] have shown similar results.

Images made of the refractive index using the time-of-flight method exhibit a better quality than those made of the attenuation coefficient. The estimate of the attenuation coefficient is obtained from the power spectrum of the received pulse. Dines and Kak [11], Lizzi and Coleman [12], Kuc *et al.* [13], and others have recognized that the power spectrum is degraded due to the presence of multipath in the received waveform. The result of this degradation is to cause errors in the measurement of the attenuation coefficient. It should be noted that the same multipath that causes the error in the attenuation estimate only barely affects the time-of-flight estimate.

This paper will show two methods to reduce the effects of multipath in reconstructions based on the attenuation coefficient. The first model assumes that multipath causes a multiplicative noise called scalloping to appear in the received power spectrum. Techniques based on homomorphic signal processing [14] will be applied to correct for the noise. The second model assumes that multipath causes samples in the projections, corresponding to paths near boundaries within the object, to contain impulse-like noise. The second correction method is an application of the non-linear technique of median filtering [15] which forces the projections to be smooth.

Section 2 will present a review of the estimation techniques used in time-of-flight and attenuation tomography. A discussion of multipath artifacts will be presented in Section 3. The correction techniques will be developed in Section 4. Section 5 contains the results of an experimental study to check the effectiveness of the correction methods.

2. PARAMETER ESTIMATION

A tomogram is a map of one of the characteristics of an object on a plane. In ultrasound tomography, the characteristics of interest are the refractive index and the ultrasonic attenuation coefficient of the object. Consider a two-dimensional function that represents the characteristic of the object in a plane. Assume for the moment that integrals of this function along straight lines can be obtained. If these integrals are known for all paths through the function then they can be inverted to recover the original function. The reconstruction algorithm using these line integrals is based on the well known theory of projections [16].

Tomography using any kind of energy can be achieved if the straight-line integrals can be determined. The estimation of line integrals for ultrasonic tomography can be achieved only if many assumptions, dealing with the interaction of sound with an object, are made. Section 2.1 presents the assumptions necessary so that the interaction of sound with an object satisfies the requirements of the reconstruction algorithm. Based on the model shown in 2.1, Sections 2.2 and 2.3 present methods to estimate line-integrals of acoustic parameters.

2.1 Model for sound interaction with an object

Consider the object slice depicted in figure 1. The medium outside the slice is water. The slice is interrogated via an incident field generated by the transmitting

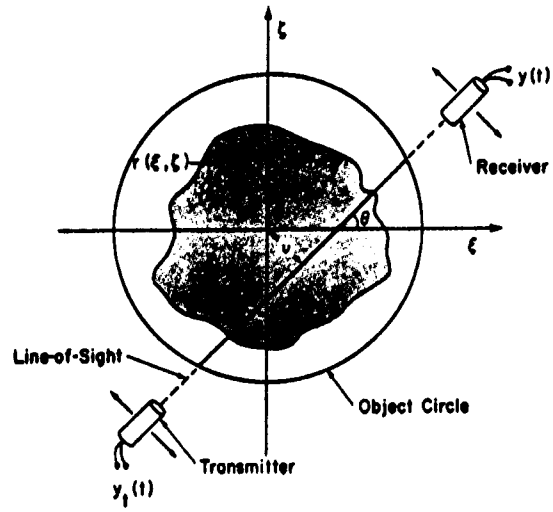

Fig. 1 Transducer configuration for the estimation of projection samples.

transducer. The forward propagated field is measured by the receiving transducer. The straight line connecting the centers of the two transducers is called the line-of-sight path.

The final result of the estimation process is a line integral along the line-of-sight path. Ultrasound should also travel along this path. This criterion is partially satisfied if the wavelength of the incident field is much less than the correlation length of the object. This situation is the acoustic analogy to geometrical optics where the energy is assumed to propagate along rays. The path of each ray is governed by the laws of refraction. Diffraction effects will be present if the ray model does not hold. These effects are beyond the scope of this paper and hence will not be considered.

The desired path of propagation for the ultrasound is the line-of-sight path between the two transducers. Refraction will cause the ray to deviate from this path. Ray bending will not occur if the boundaries within the object are perpendicular to the direction of propagation. Consider a cylinder of a few wavelengths in diameter whose central axis is the line-of-sight path. The assumption of perpendicular incidence implies that the cylinder contains a stack of homogeneous layers. The faces of the layers are all parallel to each other and perpendicular to the central axis.

The transmitter can emit a number of rays all of which can be incident on the object. It is possible for rays to travel along different paths within the object and still reach the receiver. This condition is known as multipath. Multipath can be avoided if the cylinder described above has its diameter extended so that the cylinder always contains the incident beam. The ray traveling along the line-of-sight path will be the only ray to reach the receiver.

Assume that the model just presented is correct for the object shown in figure 1. The transmitting transducer is excited with the waveform $y_t(t)$. The corresponding waveform at the output of the receiver is $y(t)$. It has been shown that with the assumptions of both linear and geometric propagation that the Fourier transforms of $y_t(t)$ and $y(t)$, $Y_t(f)$ and $Y(f)$, respectively, can be related through the following equation [4]

$$Y(f) = K\,Y_t(f)\,H_t(f)\,H_r(f)\exp\left[-\int_0^{\mu_1}[\alpha(\mu,f) + j\beta(\mu,f)]d\mu\right] , \tag{1}$$

where K is the specular transmission coefficient. $H_t(f)$ and $H_r(f)$ are the transfer functions of the transmitting and receiving transducers, respectively. The terms α and β are the attenuation and phase coefficients, respectively. The variable μ is a distance measure along the line-of-sight path between the two transducers. $\mu=0$ is at the face of the transmitter and $\mu=\mu_1$ is at the face of the receiver.

Implicit in the derivation of (1) is the assumption that the phase of the received field is constant across the face of the receiving transducer. Phase cancellation errors will occur if the phase is not constant when the field is integrated on the surface of the receiver. The errors that result from phase cancellation are basically sampling theorem problems. We make the assumption that our sampling intervals are small enough so that phase cancellation can be ignored and that any remaining artifacts are secondary.

Consider the signal received when the object is removed and replaced with water. This signal is called the water path signal and is denoted by $y_w(t)$. Its Fourier transform, $Y_w(f)$, is given by

$$Y_w(f) = Y_t(f)\,H_t(f)\,H_r(t)\exp\left[-\int_0^{\mu_1}[\alpha_w(f) + j\beta_w(f)]d\mu\right] , \tag{2}$$

where the subscript 'w' indicates properties of water.

Now substitute (2), into (1) to obtain a description of the received signal in terms of the water path signal. The result is

$$Y(f) = K Y_w(f)\exp\left[-\int_0^{\mu_1}\{[\alpha(\mu,f)-\alpha_w(f)] + j[\beta(\mu,f)-\beta_w(f)]\}d\mu\right] . \tag{3}$$

Over the frequency range used in diagnostic imaging, soft tissue has been shown to be dispersionless [17-18]. The phase coefficients $\beta(\mu,f)$ and $\beta_w(f)$ reduce to

$$\beta(\mu,f) = \frac{2\pi f}{v(\mu)} \tag{4}$$

$$\beta_w(f) = \frac{2\pi f}{v_w} , \tag{5}$$

where v and v_w are the phase velocities of sound within the object and water, respectively.

Using (4) and (5), (3) can be reduced to

$$Y(f) = K Y_w(f)\exp\left[-\int_0^{\mu_1}[\alpha(\mu,f) - \alpha_w(f)]d\mu\right]\exp(-j2\pi f\tau) , \tag{6}$$

where

$$\tau = \frac{1}{v_w}\int_0^{\mu_1}(n(\mu) - 1)d\mu , \tag{7}$$

and $n(\mu)$ is the refractive index defined by

$$n(\mu) = \frac{v_w}{v(\mu)} . \tag{8}$$

For most biological tissues the attenuation coefficient can be modeled as [19-21]

$$\alpha(\mu,f) = \alpha_s(\mu)f^{\gamma(\mu)} \quad , \tag{9}$$

where α_s is called the slope of the attenuation coefficient. Also assume that the attenuation due to water is negligible. Eq. (6) reduces to

$$Y(f) = KY_w(f)\exp\left[-\int_0^{\mu_1}\alpha_s(\mu)f^{\gamma(\mu)}d\mu\right]\exp(-j2\pi f\tau) \quad . \tag{10}$$

Now assume that the spatial dependence of γ can be ignored

$$\int_0^{\mu_1}\alpha_s(\mu)f^{\gamma(\mu)}d\mu = \psi f^{\gamma} \quad , \tag{11}$$

where

$$\psi = \int_0^{\mu_1}\alpha_s(\mu)d\mu \quad . \tag{12}$$

The final result is that a simple transfer function relates $Y(f)$ to $Y_w(f)$

$$H(f) = K\exp(-\psi f^{\gamma})\exp(-j2\pi f\tau) \quad . \tag{13}$$

The integrals describing τ (Eq. (7)) and ψ (Eq. (12)) represent the line integrals required by the reconstruction algorithm. Thus, if τ and ψ can be estimated from the transfer function given in (13), then tomographic reconstructions can be made for the refractive index and for the slope of the attenuation coefficient. Section 2.2 describes techniques to estimate τ and Section 2.3 presents an estimator of ψ.

2.2 Estimation of τ

Assume that $Y_w(f)$ is narrow band with respect to $H(f)$. Then (13) reduces to

$$y(t) = K' y_w(t-\tau) \quad , \tag{14}$$

where

$$K' = K\exp(-\psi f') \tag{15}$$

and f' is the center frequency of $Y_w(f)$. From (14) it can be seen that the received signal is just a scaled and time shifted version of the water path signal. The term τ is the time relative to the water path signal that it takes for a signal to propagate from the transmitter to the receiver. τ can then be considered a time-of-flight measure for the signal. Because τ is linearly related to the integral of the refractive index, tomograms constructed via the direct estimation of it are called time-of-flight tomograms.

The problem of estimating τ is analogous to the radar or sonar problem of estimating the range. The optimum estimator in the presence of additive white Gaussian noise is a correlation detector, if the maximum likelihood criterion is applied [22]. However, it is extremely difficult to implement this estimator. Many authors have suggested using a less optimal, but more easily implemented, detection scheme to measure τ [7-10]. An approximate estimate of τ is found by determining the time at which the absolute value of the received signal crosses a threshold set just above the level of the background noise

$$\min t \left|_{|y(t)|>\varepsilon_{th}} \quad , \tag{16}$$

where ε_{th} is the threshold value. This method has the advantage of a simple implementation in hardware. A block diagram of the system to estimate τ is shown in figure 2.

Fig.

Fig.

wind
bott
filte

this
bori
bori
deci
ant

mat
and
pha
the
wer

is J
to fi
inva
mec
that
also

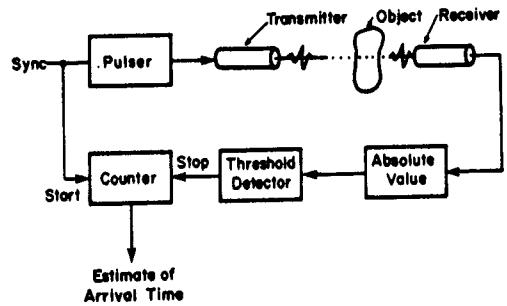

Fig. 2 Hardware implementation of time-of-flight tomography.

One source of error in the arrival-time estimate is caused by the term given by K' in (14). The effect of this term is to introduce a variable gain into the signal path. Because the threshold value is fixed, the arrival-time estimate will be a function of K'. This effect is equivalent to the case with a fixed gain and a variable threshold value. This can be explained with the help of figure 3. The top frame in figure 3 depicts a typical received signal. The absolute value of the signal is presented in the middle frame. The threshold level is the left scale in this frame. Two thresholds are indicated by the horizontal dashed lines. The arrival time as a function of the threshold is shown in the bottom frame.

The phenomenon called time-walk is the change in the measured arrival time caused by the finite rise time of the lobes of $|y(t)|$. This is seen by the linear change in the arrival time as the threshold value intercepts different parts of a lobe. When the threshold reaches the first dashed line, the measured arrival time will exhibit a jump called a time-hop. Time-hops can be eliminated by determining the arrival time of the envelope of the received signal. Time-walks can be removed if an adaptive threshold is used [23].

2.3 Estimation of ψ

The integral of the slope of the attenuation coefficient, ψ, can be estimated by considering the power spectrum of the received signal. From (13) it is given by

$$|Y(f)|^2 = K^2 |Y_w(f)|^2 \exp(-2\psi f') \quad . \tag{17}$$

The method for estimating the integrated attenuation coefficient is based on a specific model for the power spectrum of the received signal. Dines and Kak [5] and Kuc *et al.* [13] observed that if the power spectrum of the water path signal can be modeled by a Gaussian function, then the received waveform will also be Gaussian. The difference in the center frequencies between the water path power spectrum and the received power spectrum is linearly related to the integral of the attenuation coefficient.

Assume that the power spectrum of the water path signal is given by

$$|Y_w(f)|^2 = A' \exp\left[-\frac{1}{2}\left(\frac{f-f_0}{\sigma}\right)^2\right] \quad , \quad f \geq 0 \quad , \tag{18}$$

where A', f_0, and σ are parameters that characterize the Gaussian model. Now substitute (18) into (17) to determine the power spectrum of the received signal

$$|Y(f)|^2 = C \exp\left[-\frac{1}{2}\left(\frac{f-f_1}{\sigma}\right)^2\right] \quad , \quad f \geq 0 \quad , \tag{19}$$

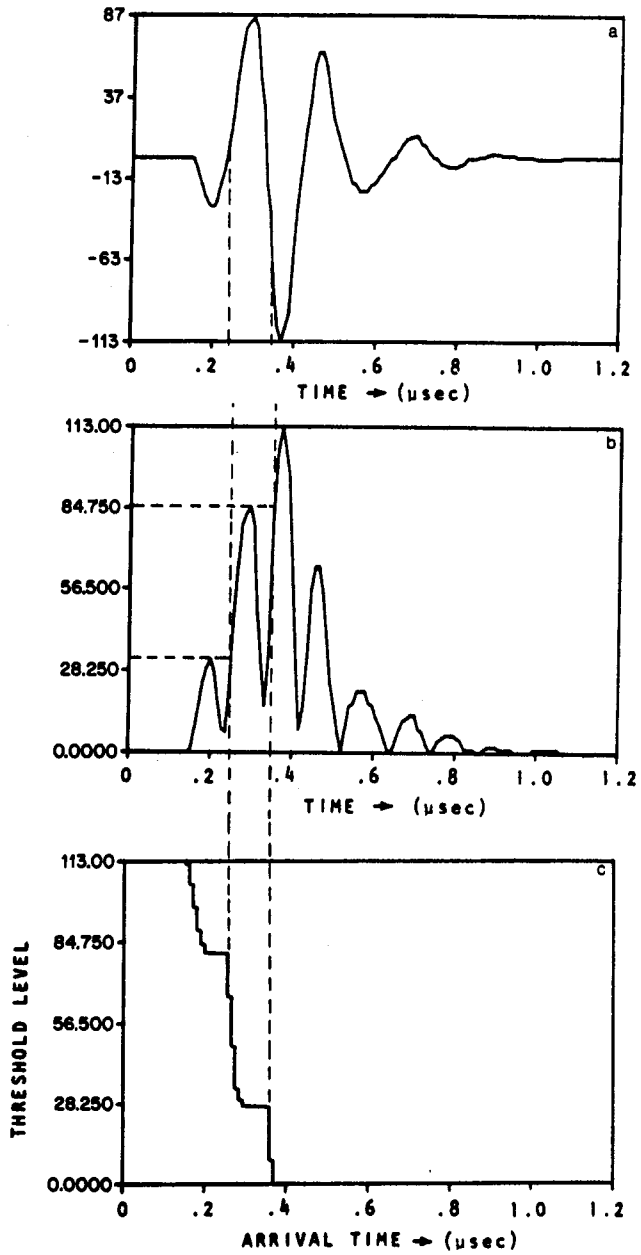

Fig. 3 Time-walk and time-hop in arrival-time estimates. (a) Received signal. (b) Absolute value of (a). (c) Arrival-time as a function of the threshold value.

where it has been assumed that γ is unity, C is a constant, and

$$\psi = \frac{f_0 - f_1}{2\sigma^2} . \tag{20}$$

It can be seen from Eq. (20) that ψ is linearly related to the shift in the center frequency from that of the water path signal to that of the received signal. Hence the name frequency shift method is given to this technique.

An estimate of the center frequency of a Gaussian function can be found by determining its mean [11]. The mean can be determined from the normalized first moment. The normalized first moment of the received power spectrum, η_Y, is defined by

$$\eta_Y = \frac{M_1}{M_0} , \tag{21}$$

where

$$M_i = \int_0^{\infty} f^i |Y(f)|^2 df \quad , \; i = 0,1 \quad . \tag{22}$$

M_0 and M_1 are called the zero and first moments, respectively. ψ can be determined by substituting η_Y for f_1 in (20).

3. MULTIPATH ARTIFACTS

In Section 2 estimators for the integrated refractive index and for the integrated slope of the attenuation coefficient were derived. Two assumptions were made in order to derive these estimators. In this section we show that it is impossible for an object to completely satisfy one of the assumptions. Multipath arises because this assumption is not met. Curved rays travel between the two transducers due to refraction. In Section 3.1 a model for the propagation of sound will be presented that incorporates multipath and refraction effects. Using this model, Section 3.2 presents a discussion of multipath artifacts.

3.1 Multipath model for sound interaction

The first assumption used in Section 2 was that the wavelength of the incident field must be much less than the correlation length of the object. The acoustic energy can be considered to propagate along rays if this assumption is satisfied. The paths of the rays are governed by the laws of refraction. Without further assumptions, there is no guarantee that only one ray will reach the receiver and that this single ray travels along the line-of-sight path.

The transmitting transducer emits a number of rays which are incident on the object. It is possible for more than one ray to reach the receiver. In Section 2 it was assumed that all the boundaries across the beam width are perpendicular to the direction of propagation. With this assumption only the ray traveling along the line-of-sight path will reach the receiver.

It is obvious that there is no way for the boundaries to be perpendicular to the direction of propagation across the beam width for every possible line-of-sight path within an object. The implication of this assumption not being satisfied is that multiple signals can reach the receiver. The paths that the individual signals travel are not straight because of refraction.

We now reconsider the model for the propagation of sound that was presented in the previous section. Assume that multipath is not present in the received waveforms. From Section 2, the received signal, y(t), is given by

$$y(t) = y_w(t) * h(t) \; , \tag{23}$$

where $y_w(t)$ is the water path signal, * indicates convolution, and the filter h(t) is given by

$$h(t) = \int_{-\infty}^{\infty} K \exp(-\psi |f|^{\gamma} - j2\pi f[\tau - t]) df \; . \tag{24}$$

The terms τ and ψ are related to the line integrals (along the line-of-sight path between the transmitter and the receiver) of the refractive index and the attenua-

tion coefficient, respectively. The term K is the specular transmission coefficient.

Now assume that multipath is present. The received signal, $y_m(t)$, will consist of M components. Each component corresponds to a signal traveling along a different path. Eq. (23) can be extended to include multipath as follows

$$y_m(t) = \sum_{i=1}^{M} y_w(t) * h_i(t) \ , \tag{25}$$

where the Fourier transform of $h_i(t)$, $H_i(f)$, is given by

$$H_i(f) = K_i \exp(-\psi_i |f|^\gamma - j2\pi f\tau_i) \ . \tag{26}$$

The terms ψ_i and τ_i are determined by integrating the corresponding object characteristic along the i'th path. Refraction is implicitly included because the ray paths are not necessarily straight.

3.2 Effect of multipath on acoustic parameter estimates

First consider the estimation of the relative arrival time τ. τ is estimated by finding the first instance of time at which the absolute value of y(t) crosses a threshold. The arrival time can be estimated by substituting the multipath corrupted received signal given by (25) into (16)

$$\min t \Big|_{|\sum_{i=1}^{M} y_w(t) * h_i(t)| > \varepsilon_{th}} \ . \tag{27}$$

It is easy to see from (27) that in most situations the output of the estimator will be the minimum value of τ_i. The attenuation terms K_i and ψ_i corresponding to the fastest signal might cause the maximum amplitude of this path to be less than ε_{th}. In this case the output of the estimator will be the next smallest value of τ_i. Thus, one sees that the result of time-of-flight estimator in the presence of multipath is always a valid estimate for the arrival time of one of the components of the received signal. Of course the arrival time estimate can be degraded by time-walk and time-hop as described in Section 2.

Now consider the estimation of the attenuation coefficient ψ_i. With the frequency shift method the attenuation estimate is made from the power spectrum of the received signal. The power spectrum of the multipath version of y(t) can be obtained by taking the square of the magnitude of the Fourier transform of (25)

$$|Y(f)|^2 = |Y_w(f)|^2 |\sum_{i=1}^{M} K_i \exp(-\psi_i |f|^\gamma - j2\pi f\tau_i)|^2 \ . \tag{28}$$

Assume that the attenuation coefficient of the l'th path is desired. The power spectrum of the signal corresponding to this path can be determined by rearranging the right-hand side of (28)

$$|Y(f)|^2 = |Y_l(f)|^2 S(f) \ , \tag{29}$$

where the multiplicative term S(f) is called the scallop function. The scallop function is given by

$$S(f) = |\sum_{i=1}^{M} \frac{K_i}{K_l} \exp(-(\psi_i - \psi_l)|f|^\gamma - j2\pi f(\tau_i - \tau_l))|^2 \ . \tag{30}$$

If $K_l \gg K_i$ and $\psi_l \ll \psi_i$, $i \neq l$, then

$$|Y(f)|^2 \approx |Y_l(f)|^2 \ . \tag{31}$$

Thus, when one of the received signals dominates the others, the power spectrum of the composite signal will be approximately the power spectrum corresponding to the strongest path. A correct attenuation estimate can be found for this path.

If one of the received signals does not dominate the others then it is obvious from (29) that the estimate of the attenuation coefficient will be a complicated

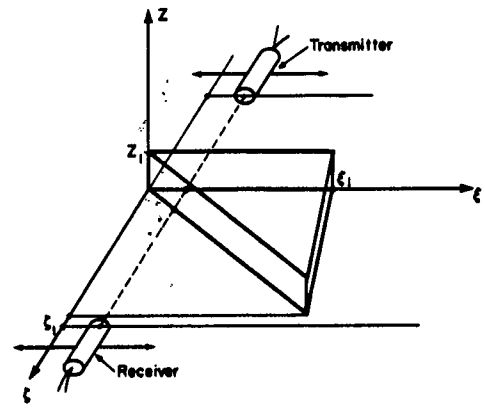

Fig. 4 Object used to study multipath artifacts.

function of all the K_j, ψ_j, and τ_j. The estimate will not necessarily be equal to any one of the ψ_j.

From this preliminary discussion, it seems that multipath will effect attenuation tomography more than time-of-flight tomography. This observation is consistent with observations in the literature [11-13].

We now consider an example in which the effects of multipath on refractive index measurements and on integrated attenuation coefficient estimates are compared. The comparison is done by evaluating the propagation of ultrasound through the triangular wedge depicted in figure 4. The object shape and the transducer positions relative to the object were chosen so that received signals with varying amounts of multipath can be generated. The assumption of the object being invariant in the direction perpendicular to the scan plane has been violated on purpose in order to introduce a well defined source of multipath errors.

The wedge is assumed to be a homogeneous piece of tissue equivalent material immersed in water. The object is characterized by a refractive index n_0 and an attenuation coefficient $\alpha(f)$ given by

$$\alpha(f) = \alpha_s |f| \ . \tag{32}$$

The two transducers are translated along lines parallel to the ξ axis. The centers of the transducer faces are in the (ξ,ζ) plane. Thus the line-of-sight path between the two transducer centers is also in the (ξ,ζ) plane. Let the ξ intercept of the line-of-sight path denote the position of the transducer pair. In this example it will be assumed that half the transmitted energy goes through the water and the other half through the wedge.

Consider positions of the transducers for $0 \le \xi \le \xi_1$. It is assumed that the output of the receiving transducer, $y(t)$, is given by the sum of two components

$$y(t) = y_w(t) + y_o(t) \ , \tag{33}$$

where $y_w(t)$ is the water path signal and $y_o(t)$ is the signal that arises from the path through the object.

In Section 2 it was shown that $y_o(t)$ can be written as

$$y_o(t) = y_w(t) * h(t) \ , \tag{34}$$

where * indicates convolution, and the Fourier transform of $h(t)$, $H(f)$, is given by

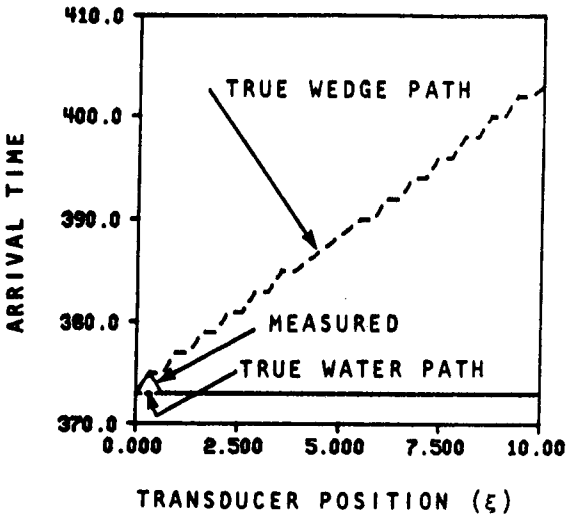

Fig. 5 Arrival time versus transducer position for the object shown in figure 4. Sound travels slower in the object than in the surrounding water. Long dashed line is the ideal arrival-time for the wedge path. Short dashed line is the ideal arrival-time for the water path.

$$H(f) = \exp(-\psi|f| - j2\pi f\tau) \ . \tag{35}$$

The term ψ is the integrated attenuation coefficient given by

$$\psi = \alpha_o \frac{\xi\zeta_1}{\xi_1} \ . \tag{36}$$

The term τ is the arrival time relative to the water path signal. The arrival time is given by

$$\tau = \frac{1}{v_w}(n_o - 1)\frac{\xi\zeta_1}{\xi_1} \ , \tag{37}$$

where v_w is the velocity of sound in water.

Assume that the water path signal is a Gaussian pulse with a center frequency of f_0

$$y_w(t) = (2\pi)^{-\frac{1}{2}}\sigma_t^{-1}\exp\left[-\frac{1}{2}\left(\frac{t-t_1}{\sigma_t}\right)^2\right]\cos 2\pi f_0(t-t_1) \ , \tag{38}$$

where σ_t is the standard deviation of the envelope. The arrival time, t_1, is assumed to be large enough so that $y_w(t) \approx 0$ for $t < 0$. This insures that $y_w(t)$ is causal.

The Fourier transform of $y_w(t)$, $Y_w(f)$, is given by [24]

$$Y_w(f) = \frac{1}{2}\exp\left[-\frac{1}{2}(2\pi\sigma_t)^2(|f| - f_0)^2 - j2\pi f t_1\right] \ , \tag{39}$$

where it has been assumed that f_0 is large enough so that the tails of the replicas of the spectrum that cross the frequency origin can be ignored.

The Fourier transform of $y_o(t)$, $Y_o(f)$, can be determined by substituting (35) and (39) into the Fourier transform of (34)

$$Y_o(f) = \frac{c}{2}\exp\left[\frac{1}{2}(2\pi\sigma_t)^2[(|f|-f_1)^2 - j2\pi f(\tau + t_1)]\right] . \tag{40}$$

where

$$f_1 = f_0 - \frac{\psi}{(2\pi\sigma_t)^2} \tag{41}$$

$$c = \exp\left[-\frac{1}{2}(2\pi\sigma_t)^2(f_0^2 - f_1^2)\right] . \tag{42}$$

The received signal, y(t), can be found by substituting (38) and the inverse Fourier transform of (40) into (33)

$$\begin{aligned} y(t) = {} & (2\pi)^{-\frac{1}{2}}\sigma_t^{-1}\exp\left[-\frac{1}{2}\left(\frac{t-t_1}{\sigma_t}\right)^2\right]\cos 2\pi f_0(t-t_1) \\ & + c(2\pi)^{-\frac{1}{2}}\sigma_t^{-1}\exp\left[-\frac{1}{2}\left(\frac{t-\tau-t_1}{\sigma_t}\right)^2\right]\cos 2\pi f_1(t-\tau-t_1) . \end{aligned} \tag{43}$$

3.2.1 Effect of multipath on the time-of-flight estimate

The arrival time is determined by substituting (43) into (16). There are two distinct cases for the arrival time. One case is when the speed of sound in the water is faster than in the wedge. The other case is when the speed of sound is faster in the wedge than in the surrounding water.

Consider first the case when the object is slower than the water. The object being slower implies that $n_o > 1$ and hence $\tau > 0$. Thus the signal traveling through the wedge will always arrive at a time later than that of the water path signal. The water path signal never gets attenuated in this model. Thus, the arrival time estimate will always be a measurement of the arrival time of the water path signal. Some degradations in the arrival time occur for small values of τ. This is because the initial portion of the object path signal can interfere with the water path signal where the threshold would be crossed if the object path was not present. This effect can be seen in figure 5 where the arrival time versus ξ is plotted. The deviation from the correct arrival time for small ξ is due to the interaction of the two components of y(t).

Now consider the opposite situation in which sound travels faster in the object than in the water. In this case τ is negative and hence the signal traveling through the object arrives before the water path signal. Thus the arrival time estimate will be made on the object path signal. This will be true if the maximum value of the object signal is greater then the threshold value. The object path signal is attenuated as the transducers are translated from $\xi = 0$ to $\xi = \xi_1$. Thus, it is possible for the maximum value of $y_o(t)$ to fall below the value of ε_{th}. When this happens, the arrival time estimate will be made from the water path signal. This effect is seen in figure 6 where the arrival time is plotted as a function of ξ. The threshold value ε_{th} is set so that half-way through the traverse the maximum value of $y_o(t)$ is less than ε_{th}. This causes the large discontinuity in the arrival time. This is known as a time-hop due to multipath. The other deviations from the correct arrival time for the object path are due to the time-hop and time-walk as described in Section 2.

From the previous two examples it can be seen that the arrival time estimate is a valid estimate for one of the two paths for all values of ξ. This will now be contrasted to the attenuation estimate.

3.2.2 Effect of multipath on the attenuation estimate

The attenuation coefficient will be estimated using the frequency shift method. The power spectrum of the received signal, $|Y(f)|^2$, can be found by first finding the square of the magnitude of the Fourier transform of (43)

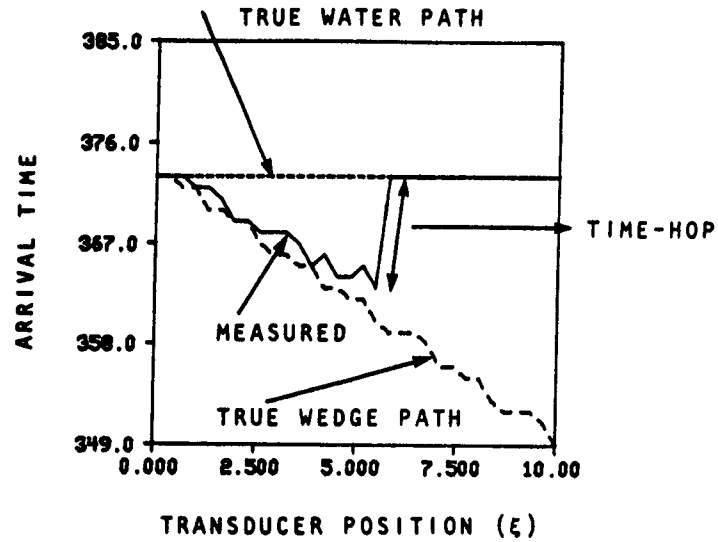

Fig. 6 Arrival time versus transducer position for the object shown in figure 4. Sound travels faster in the object than in the surrounding water. Long dashed line is the ideal arrival-time for the wedge path. Short dashed line is the ideal arrival-time for the water path.

$$|Y(f)|^2 = \frac{1}{4}\exp\left[-\frac{1}{2}\left(\frac{|f|-f_0}{\sigma}\right)^2\right] + \frac{c^2}{4}\exp\left[-\frac{1}{2}\left(\frac{|f|-f_1}{\sigma}\right)^2\right] + A\exp\left[-\frac{1}{2}\left(\frac{|f|-\bar{f}}{\sigma}\right)^2\right]\cos 2\pi f\tau \tag{44}$$

where

$$\bar{f} = \frac{f_0 + f_1}{2} \tag{45}$$

$$A = \frac{c}{2}\exp\left[\frac{f_1^2 + f_0^2 - 2\bar{f}}{4\sigma^2}\right] . \tag{46}$$

Now substitute (44) into (21)

$$f_c = \frac{f_0 + c^2 f_1 + 4A\exp\left[-\frac{1}{2}(2\pi\tau\sigma)^2\right](\bar{f}\cos 2\pi\tau\bar{f} - \sigma^2 2\pi\tau\sin 2\pi\tau\bar{f})}{1 + c^2 + 4A\exp\left[-\frac{1}{2}(2\pi\tau\sigma)^2\right]\cos 2\pi\tau\bar{f}} . \tag{47}$$

The center frequency determined with (47) can be substituted for f_1 in (20) to obtain the value of ψ that is estimated in the presence of multipath. Figure 7 shows a plot of this estimate as the two transducers are translated across the extent of the wedge. For small values of ξ the estimate does not correspond to the attenuation coefficient for either the water path or the object path. At these values of ξ, the relative delay, τ, is close to zero and hence the sinusoidal terms in (47) dominate.

As ξ increases, the object path is attenuated to the point where it is negligible with respect to the water path signal. When this happens, the attenuation estimate is made from only the water path which has zero attenuation in the path.

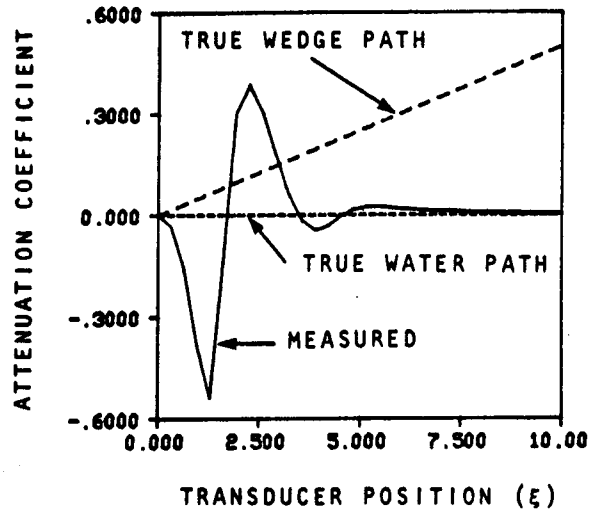

Fig. 7 Attenuation coefficient estimate versus transducer position for the object shown in figure 4. Long dashed line is the ideal attenuation coefficient for the wedge path. Short dashed line is the ideal attenuation coefficient for the water path.

We saw previously that the time-of-flight estimator always yields a correct estimate for either the water or the wedge path. The attenuation estimator at small values of ξ produces an estimate that is not consistent with either of the two paths. It is obvious that the knowledge that an estimate is valid for one of the two paths is better than not having a valid estimate of either of the paths. Thus, this example has demonstrated that in the presence of multipath the attenuation estimator performs worse than the time-of-flight estimator. This is consistent with the intuitive results presented in the beginning of this section.

4. CORRECTIONS FOR MULTIPATH

In the previous section it was shown how the presence of multipath affects refractive index and attenuation tomograms. Even though multipath affects both types of tomograms, it has a more severe effect on attenuation tomograms. In this section we show methods to reduce the influence of multipath on attenuation tomograms.

There are two ways to consider multipath within the context of this project. The first method is to treat each received waveform as a separate identity. One then tries to recover the uncorrupted power spectrum of one of the components that comprise the received signal. Techniques to perform this task are presented in Section 4.1.

With the second multipath correction method, one forms projections of the object assuming that multipath is not present in the received waveforms. The presence of multipath causes irregularities in the projection space. The non-linear filtering method presented in Section 4.2 is used to remove the inconsistencies.

4.1 Homomorphic filtering

The problem of multipath in transmission tomography is analogous to clutter in radar or sonar [25], multiple reflections in ultrasonic echo tomography [26], and

reverberations in seismic exploration [27]. In all of these situations the received signal can be approximately modeled by the convolution of the desired signal with a train of impulses. One needs to deconvolve the unknown impulse train to recover the desired signal. Because the desired signal is also unknown, classical deconvolution techniques are not applicable. The generalized inverse filtering method called homomorphic filtering has been used to perform the deconvolution operation in these situations [28-31]. In this section we demonstrate that homomorphic filtering is also applicable for the removal of multipath artifacts in ultrasonic tomography.

What follows is a brief introduction to homomorphic signal processing. A more complete description can be found elsewhere [14].

Consider two signals $x_1(t)$ and $x_2(t)$. Let G be an operator used to combine $x_1(t)$ and $x_2(t)$. The output of the system is given by

$$y(t) = G[x_1(t);x_2(t)] \quad . \tag{48}$$

It is desired to filter the output of the system, $y(t)$, to remove one of the two components. In general G is non-linear. Thus linear filtering is not directly applicable.

Consider the system transformation D, whose functional dependence is determined by G, that transforms the system to a linear space

$$D\Big\{G[x_1(t);x_2(t)]\Big\} = \hat{x_1}(t) + \hat{x_2}(t) \quad , \tag{49}$$

where

$$\hat{x_1}(t) = D\Big\{x_1(t)\Big\} \tag{50}$$

$$\hat{x_2}(t) = D\Big\{x_2(t)\Big\} \quad . \tag{51}$$

Because functions of the components $x_1(t)$ and $x_2(t)$ appear as a sum, linear filtering can now be used.

Apply the linear operator L to (49)

$$L\Big\{\hat{x_1}(t) + \hat{x_2}(t)\Big\} = \hat{y_1}(t) + \hat{y_2}(t) \quad , \tag{52}$$

where

$$\hat{y_1}(t) = L\Big\{\hat{x_1}(t)\Big\} \quad . \tag{53}$$

$$\hat{y_2}(t) = L\Big\{\hat{x_2}(t)\Big\} \quad . \tag{54}$$

L can be designed to remove either $\hat{x_1}(t)$ or $\hat{x_2}(t)$.

Assume that the operator D possesses an inverse D^{-1}. Then D^{-1} can be applied to (52) to return to the original signal space

$$D^{-1}\Big\{\hat{y_1}(t) + \hat{y_2}(t)\Big\} = G[\hat{y_1}(t);\hat{y_2}(t)] \quad . \tag{55}$$

D followed by L followed by D^{-1} is called a homomorphic system. The advantage of this type of system is that once D is determined, only a linear filtering problem remains.

Consider a multiplicative system. The operator G is defined by

$$G[x_1(t);x_2(t)] = x_1(t)x_2(t) \quad . \tag{56}$$

It is clear that the system transformation D is the complex logarithm. The corresponding inverse operation, D^{-1}, is the complex exponential. If the logarithm of (56) is taken, the following is obtained

$$\log(x_1(t)x_2(t)) = \hat{x_1}(t) + \hat{x_2}(t) \quad , \tag{57}$$

where

$$\hat{x_1}(t) = \log(x_1(t)) \tag{58}$$

$$\hat{x_2}(t) = \log(x_2(t)) \quad . \tag{59}$$

Thus, if two functions are combined through the operation of multiplication, then the complex logarithm can be used to transform into a linear system. A linear filter can be used to remove one of the multiplicative components.

We now show how the multiplicative model lends itself to the removal of multipath. Consider the following simplified model for multipath

$$x_r(t) = x(t) * s(t) \quad , \tag{60}$$

where * indicates convolution, $x_r(t)$ is the received signal, x(t) is the desired signal, and s(t) is the impulse train that incorporates multipath. The multipath term is defined with

$$s(t) = \delta(t) + \sum_i a_i\delta(t - b_i) \quad . \tag{61}$$

The summation in (61) is the contribution from multipath. Assume that only the power spectrum of the signal x(t) is desired. This power spectrum can be found by first finding the square of the magnitude of the Fourier transform of (60)

$$|X_r(f)|^2 = |X(f)|^2|S(f)|^2 \quad , \tag{62}$$

where

$$S(f) = 1 + \sum_i a_i\exp(-j2\pi f b_i) \quad . \tag{63}$$

When one compares (62) to (56), it is seen that in the Fourier domain multipath can be modeled as a multiplicative system. The system transformation D is accomplished by taking the logarithm of (62)

$$\hat{X_r}(f) = \hat{X}(f) + \hat{S}(f) \quad , \tag{64}$$

where

$$\hat{X_r}(f) = \log(|X_r(f)|^2) \tag{65}$$

$$\hat{X}(f) = \log(|X(f)|^2) \tag{66}$$

$$\hat{S}(f) = \log(|S(f)|^2) \quad . \tag{67}$$

$\hat{S}(f)$ can be evaluated by substituting (63) into (67)

$$\hat{S}(f) = \log(1 + \sum_i a_i\exp(-j2\pi f b_i) + \sum_i a_i\exp(j2\pi f b_i) + \sum_i\sum_j a_i a_j\exp(-j2\pi f[b_i - b_j])) \quad . \tag{68}$$

This can be further simplified with the following Taylor series expansion

$$\log(1 + x) = \sum_{k=1}^{\infty} \frac{-1^{k+1}}{k}x^k \quad , \quad |x| < 1 \quad . \tag{69}$$

Now substitute (68) into (69) and also make the assumption that only one source of multipath is present. This results in

$$\hat{S}(f) = \sum_{k=-\infty}^{\infty} c_k\exp(j2\pi f k b_1) \quad , \tag{70}$$

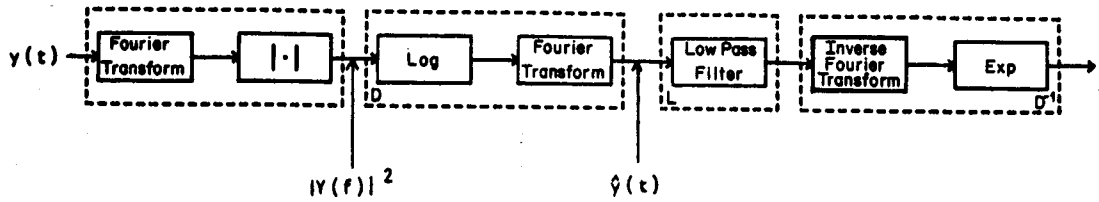

Fig. 8 Homomorphic system to recover a power spectrum.

where the c_k's are constants.

Now take the Fourier transform of (64)

$$\hat{x_r}(t) = \hat{x}(t) + \hat{s}(t) \quad . \tag{71}$$

The terms $\hat{x_r}(t)$, $\hat{x}(t)$, and $\hat{s}(t)$ are called the power cepstra corresponding to $x_r(t)$, $x(t)$, and $s(t)$, respectively. $\hat{s}(t)$ can be found by taking the Fourier transform of (70)

$$\hat{s}(t) = \sum_{k=-\infty}^{\infty} c_k \delta(t - kb_1) \quad . \tag{72}$$

The cepstrum corresponding to $x(t)$, $\hat{x}(t)$, is an even function centered about the time origin. Thus, if the duration of $\hat{x}(t)$ is less than $|b_1|$, then $\hat{x}(t)$ can be recovered by low pass filtering in the cepstrum domain. The value of $\hat{x}(t)$ at $t=0$ can not be recovered because one of the impulses given in (72) is also at this point. The value of the cepstrum at this point is related to the frequency independent gain of the system. The attenuation estimators exploit the frequency dependence of the power spectrum. Thus there is no problem if the $\hat{x}(0)$ term is not recovered.

The output of the low-pass filter can be inverse Fourier transformed and then passed through an exponential operator. The output at this stage is the recovered value of $|X(f)|^2$. The complete system needed to recover this power spectrum is shown in figure 8.

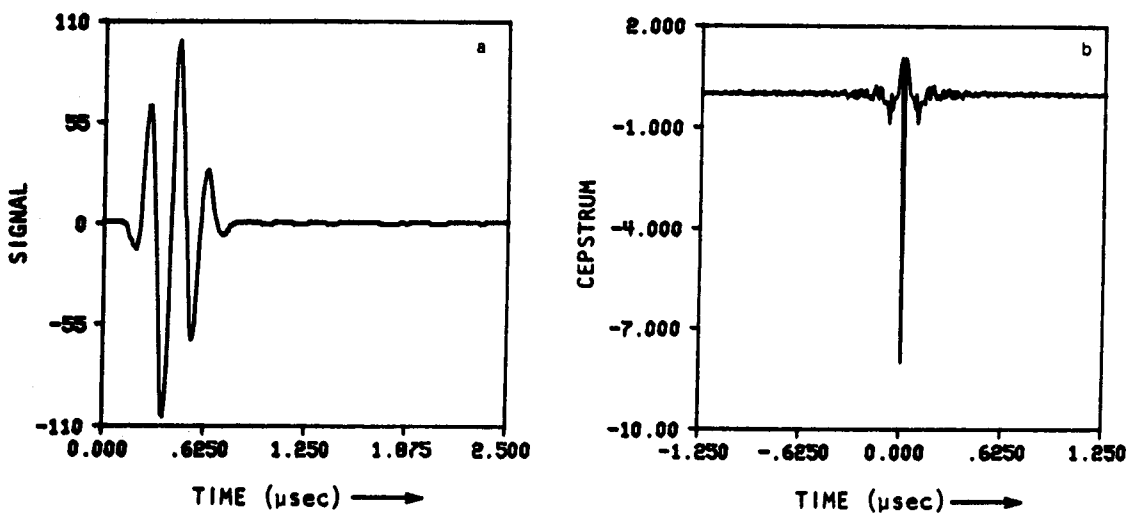

Fig. 9 (a) Typical received signal. (b) Cepstrum of (a).

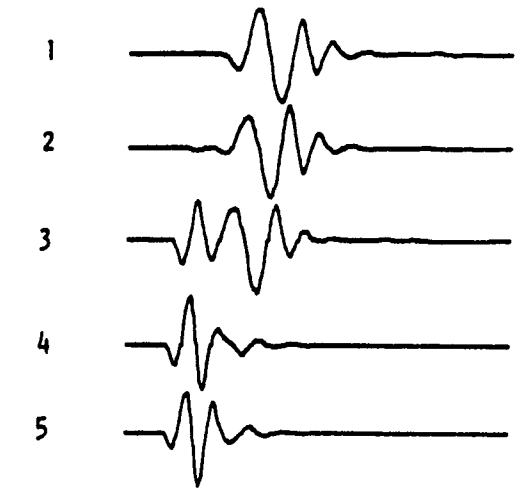

(10)

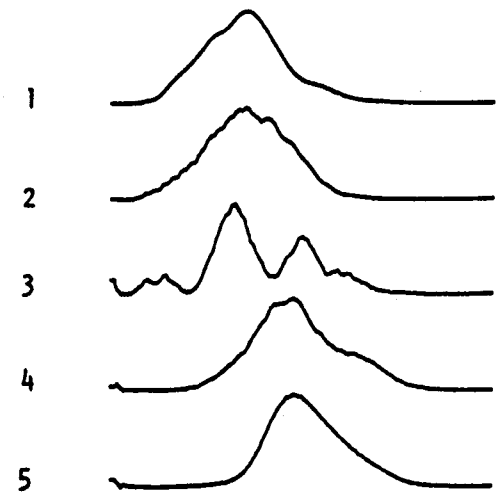

(11)

Fig. 10 Five received signals near the edge of a circular gelatin phantom.

Fig. 11 Power spectra corresponding to signals shown in figure 10.

Homomorphic filtering is useful only if the duration of the cepstrum of a signal is less than the duration of the signal itself. When this condition is not satisfied, time gating the original signal will yield better results than filtering the cepstrum of the signal. In figure 9 we show a typical received signal and its cepstrum. The duration of the cepstrum is less than the duration of the signal. Thus homomorphic filtering is applicable to ultrasonic tomography.

We now demonstrate homomorphic filtering on real signals containing multipath. The five values of $x_r(t)$ in figure 10 were obtained as a transmitter/receiver pair was scanned past the edge of a circular phantom made of an oil-based gel. In the first signal, the beam from the transmitter to the receiver is completely within the object. In the second signal, the beam is beginning to leave the object. The predominant pulse corresponds to the signal traveling trough the object. The small "blip" on the left is the contribution from the path outside the object. In the third signal, the portion received via the outside path is comparable in magnitude to the signal received from the path inside the object. Finally in the last signal, the path linking the transmitter and the receiver is completely outside the object.

The power spectra corresponding to the five signals in figure 10 are shown in figure 11. The scalloping due to multipath is slightly evident in the second power spectrum and very visible in the third since the contributions from the paths are nearly equal at this point.

The power cepstra corresponding to the five signals in figure 10 are shown in figure 12. The presence of multipath is not clear in these plots. We now digress for a moment and determine analytically the power cepstrum corresponding to a signal that has a Gaussian power spectrum. A Gaussian model is a good approximation to the power spectra of typical ultrasound signals.

Consider a signal x(t) with a Gaussian power spectrum given by

$$|X(f)|^2 = A\exp\left[-\frac{1}{2}\left(\frac{|f|-f_0}{\sigma}\right)^2\right] . \qquad (73)$$

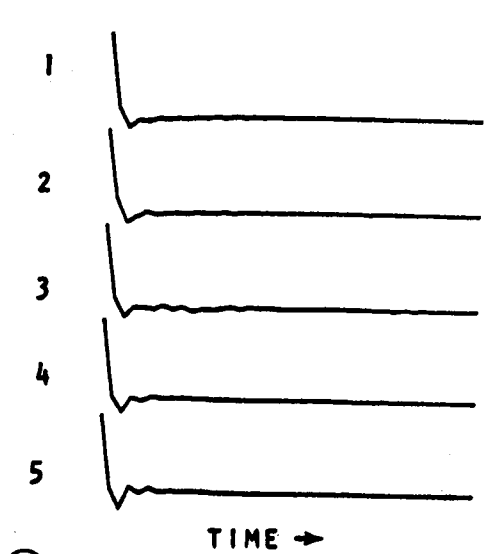

(12)

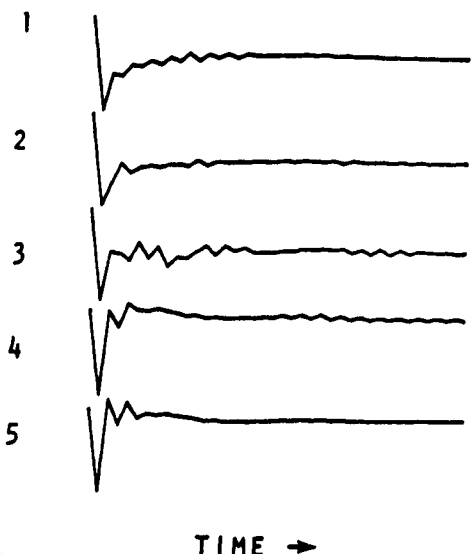

(13)

Fig. 12 Power cepstra corresponding to signals shown in figure 10.

Fig. 13 Same power cepstra that are shown in figure 12, but now the first point has been excluded.

The logarithm of the power spectrum given in (73), Z(f), is given by

$$Z(f) = a_1 f^2 + a_2 |f| + a_3 \ , \tag{74}$$

where

$$a_1 = -\frac{1}{2\sigma^2} \tag{75}$$

$$a_2 = \frac{f_0}{\sigma^2} \tag{76}$$

$$a_3 = \ln A - \frac{f_0^2}{2\sigma^2} \ . \tag{77}$$

The power cepstrum corresponding to x(t), $\hat{x}(t)$, is determined by taking the Fourier transform of (74)

$$\hat{x}(t) = \int_{-B}^{B} (a_1 f^2 + a_2 |f| + a_3) \exp(-j2\pi ft)\, df \ . \tag{78}$$

The limits on the integral are set to -B and B in order for the Fourier transform to exist. The function given in (74) is not square integrable over the region $(-\infty,\infty)$. The region (-B,B) represents the bandwidth required when samples are taken in the time domain every $\frac{1}{2B}$ seconds.

The integral in (78) can be evaluated through the use of the following relationship (eq. 2.633.2 in ref. [32])

$$\int x^n \cos ax\, dx = \sum_{k=0}^{n} k! \binom{n}{k} \frac{x^{n-k}}{a^{k+1}} \sin\left(ax + \frac{1}{2}k\pi\right) \ . \tag{79}$$

The result after substituting (79) into (78) is

$$\hat{x}(t) = \frac{2a_3 \sin 2\pi Bt}{2\pi t} + a_2\left[\frac{B \sin 2\pi Bt}{\pi t} - \left[\frac{\sin \pi Bt}{\pi t}\right]^2\right] + a_1\left[\frac{B \cos 2\pi Bt}{(\pi t)^2} + \frac{B^2 \sin 2\pi Bt}{\pi t} - \frac{4 \sin 2\pi Bt}{(2\pi t)^3}\right] . \tag{80}$$

Now consider samples that occur every $\frac{1}{2B}$ seconds. The samples occur at

$$\hat{x}_i = \hat{x}\left(\frac{i}{2B}\right) \quad , \quad i = 0,1,\ldots \tag{81}$$

The sample values can be determined by substituting (80) into (81)

$$\hat{x}_i = \begin{cases} -\frac{B^3}{6\sigma^2} + \frac{f_0 B^2}{2\sigma^2} + (\ln \Lambda - \frac{f_0^2}{2\sigma^2} B) & , \ i = 0 \\ \frac{B^3}{\pi\sigma^2 i^2}(1 - \frac{2f_0}{B}) & , \ i \text{ is odd} \\ -\frac{B^3}{\pi\sigma^2 i^2} & , \ i \text{ is even} . \end{cases} \tag{82}$$

From (82) it can be seen that all the amplitude information is contained in the $\hat{x}_0$ term. The center frequency, f_0, can be determined from the $\hat{x}_1$ term if σ is known. This is useful because when the frequency shift method is applied to estimate the attenuation coefficient, only f_0 has to be determined. This implies that only the $\hat{x}_1$ term has to be retained in the power cepstrum. It has been found though, that in the presence of noise, a few more terms have to be retained to obtain reliable estimates.

We now return to the five signals previously used as an example. In figure 13 we show the same cepstra that were shown in figure 12 but now the cepstra have been plotted without the $\hat{x}_0$ term. Eq. (82) indicates that the cepstra should approach zero with a one over i^2 dependency. Thus, the effects of multipath are the ripples on the right sides of the middle signals.

The low pass filtering step is accomplished by setting to zero all but the first three points in each cepstrum. (The zero'th terms are one of the three points.) The resulting power spectra are shown in figure 14. It is seen that the scalloping due to multipath has been removed.

4.2 Median filtering

The second way to remove multipath is to initially ignore the presence of multipath in the received waveforms. Projections of the attenuation coefficient can be formed using the estimation technique presented in Section 2. It is obvious that multipath manifests itself through errors in the projection space. In this section we show a method to remove these errors.

Consider sample values in the projection space that correspond to paths near edges within the object. Figure 15 depicts four paths within an object near edges within the phantom. It is obvious that signals received along line-of-sight paths corresponding to these four paths will be corrupted by multipath. Thus, the attenuation projection will have errors at these locations. This can be seen in figure 16 where we show a computer simulated attenuation projection of the object shown in figure 15. (The details of the computer simulation can be found in [38].) The effect of multipath is to introduce the four glitches in the projection.

It is obvious that multipath will not always cause glitch noise. When the relative arrival times for the multipath components in a signal remain approximately constant for a few samples in a projection, then the effect of multipath is a systematic error in the projection. This type of error will not appear as an incon-

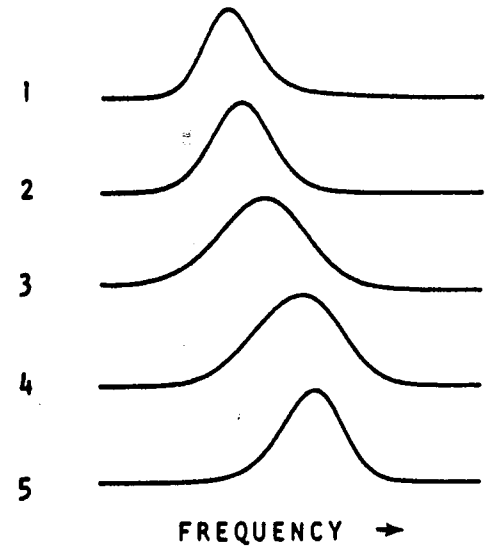

Fig. 14 Recovered power spectra after homomorphic filtering.

sistency in a projection. This situation can be seen in figure 15. Consider the two extreme glitches. Even though they do appear to be inconsistencies within the projection, they could also be considered to be valid projection values. Clearly, the errors in the middle of the projection are glitches.

Multipath can be removed if the multipath glitches can be removed from the projection. Linear filtering is not applicable for the removal of the noise because of the large bandwidth of glitch noise. The non-linear filtering method called median filtering has been shown to remove glitch noise [33-35]. We now present a short introduction to the theory of median filtering. More complete information can be found elsewhere [15].

Consider the following N-point sequence

$$x_0, x_1, \ldots, x_{N-1} \quad . \tag{83}$$

A window of length length 2J+1 centered around i is denoted with W_i^J. The window is given by the following set of points

$$W_i^J = \{x_{i-J}, \cdots, x_{i-1}, x_i, x_{i+1}, \cdots, x_{i+J}\} \quad . \tag{84}$$

The median of this window, $M(W_i^J)$, is defined to be the (J+1)'th largest (or equivalently (J+1)'th smallest) point in the set W_i^J.

The output of a median filter applied to the complete set of x_i's is defined as

$$y_i = M(W_i^J) \quad , \quad i = J, J+1, \ldots, N-J-1 \quad . \tag{85}$$

The values of y_i for $i = 0, \ldots, J-1$ and $i = N-J, \ldots, N-1$ can not be defined with this method. This is because there are an insufficient number of input points to form the window. Usually the input is passed directly to the output at these points

$$y_i = x_i \quad , \quad i = 0, 1, \ldots, J-1 \text{ and } i = N-J, \ldots, N-1 \quad . \tag{86}$$

A demonstration of median filtering is shown in figure 17. A sequence of N=12 points is presented at the top of the figure. All of the possible positions for a J=1

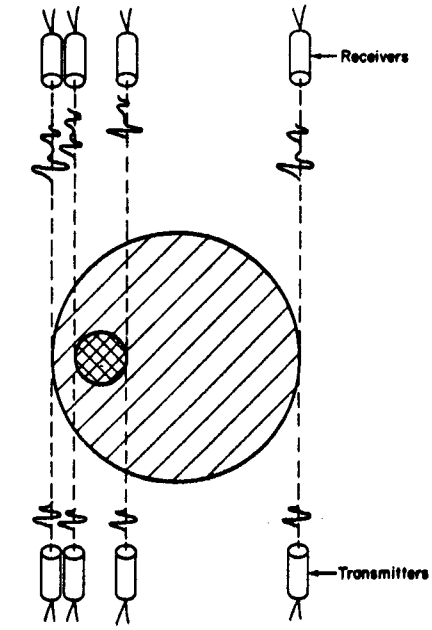

(15)

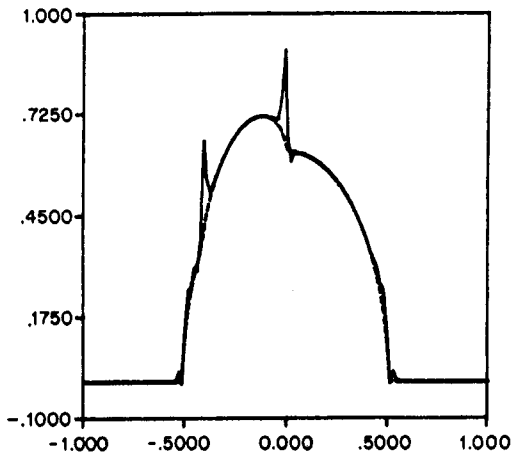

(16)

Fig. 15 Example of possible locations of ray paths that can lead to multipath distortion in the projection.

Fig. 16 Simulated projection (solid line) of object shown in figure 15. Dashed line is true projection.

window are shown in the middle. The output of the median filter is shown on the bottom (note that the output is plotted upside down). It is clear that the median filter smoothed the input waveform.

The properties of median filters have been derived in [36]. The main point of this paper is the concept of a root signal. Consider a signal that consists of neighborhoods that are either strictly monotonic or constant. The length of each neighborhood must be at least $J+1$. Also assume that between a pair of increasing and decreasing monotones there is a constant neighborhood. Then this signal is invariant to median filtering and is called a root signal.

We now demonstrate that projections of a complicated phantom are approximately root signals. Consider the computer simulated reconstruction of the Shepp and Logan head phantom [37] in figure 18. This is considered to be a very difficult phantom to image because of the large contrast between the simulated skull and the simulated tissue. Fifty projections with one-hundred samples per projection were used to obtain this reconstruction.

The projections are then filtered with a median filter. The length of the window is $J=2$. The subsequent reconstruction is shown figure 19. If this figure is compared to figure 18, one sees that the reconstructions of this complex phantom are almost invariant to median filtering. This implies that the projections are also invariant to median filtering. Thus the projections are approximate root signals. We assume that we can extend this result to speculate that projections from most objects are also root signals.

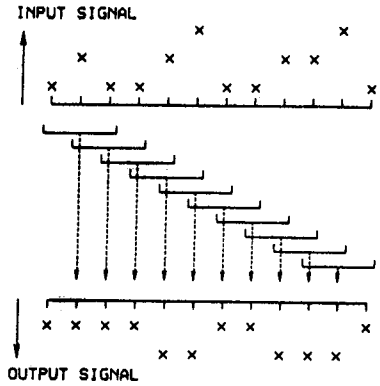

Fig. 17 Demonstration of median filtering. Top signal is the input to the filter. Bottom signal is the output of the filter.

If one compares the reconstructions presented in figures 18 and 19, it can be seen that the only difference between them is the dark area in the center of the latter reconstruction. This error also results in the large error at the center of the center-line profile shown in figure 19. This error is a result of the fact that projections of this phantom consist of a monotonically increasing section followed by a monotonically decreasing section. (Fig. 20 shows a sample projection of the Shepp and Logan phantom.) Projections of this phantom would be root signals if the two monotonic sections were separated by a constant region. The effect of a median filter on projections of this nature is to put a constant region between the two monotonic sections. This can be seen in figure 21 where the central portion of the projection shown in figure 20 is shown by the solid line. The dashed line corresponds to the central portion of the projection after it was passed through a

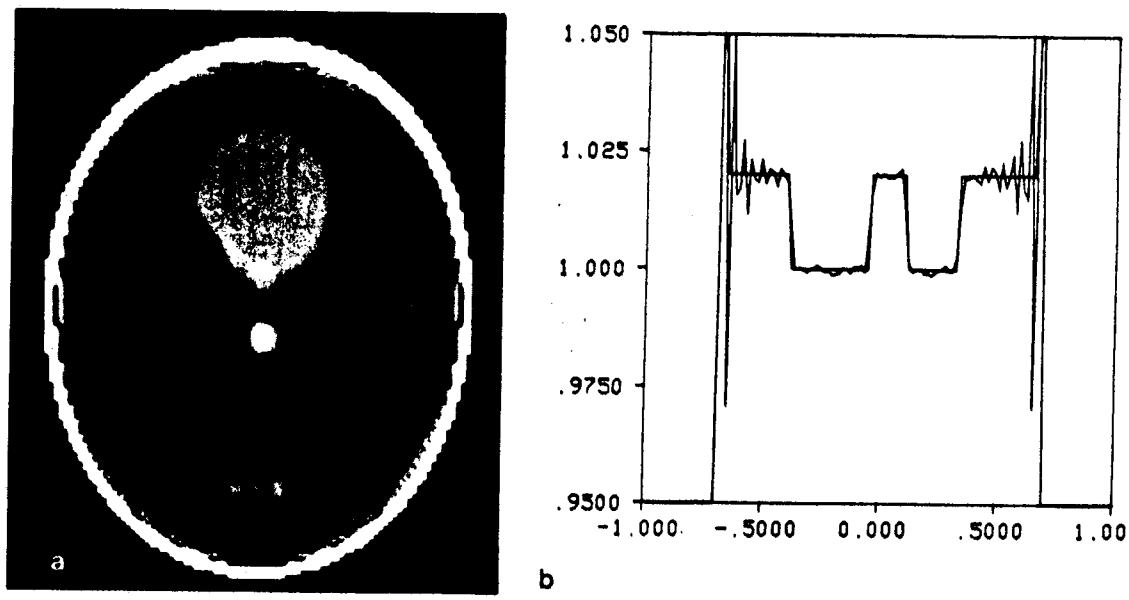

Fig. 18 Computer simulated reconstruction of the Shepp and Logan head phantom. (a) Tomogram. (b) Center-line-profile.

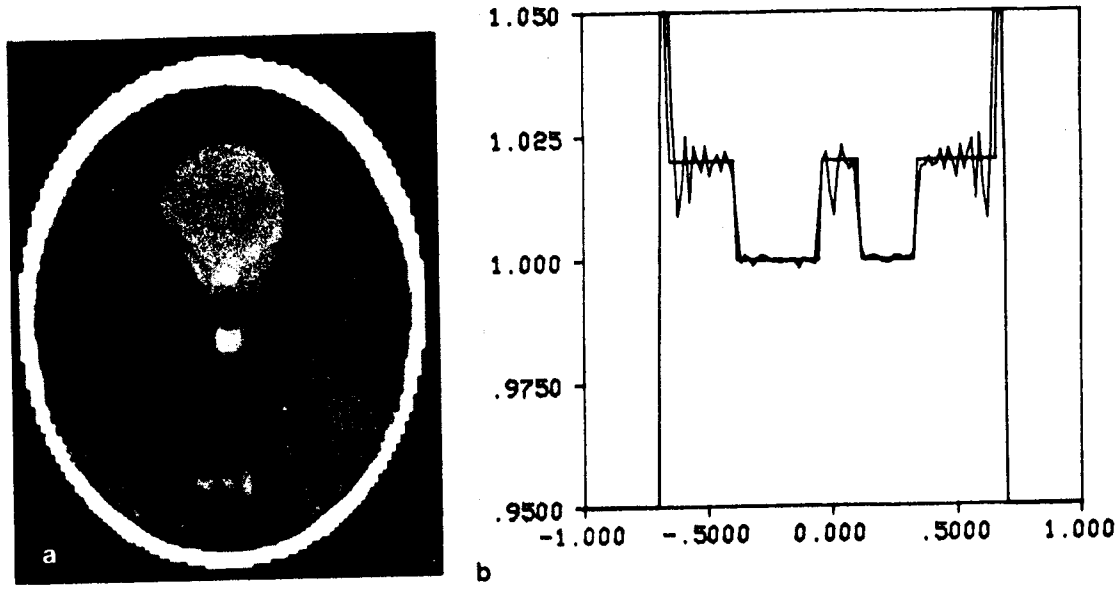

Fig. 19 Computer simulated reconstruction of the Shepp and Logan head phantom. Median filter incorporated on the projections before reconstruction. (a) Tomogram. (b) Center-line-profile.

median filter. The only difference is the constant region at the center. This discrepancy leads to the dark region in the reconstruction shown in figure 19.

Consider additive glitch noise of length less than J+1 added to different positions of a root signal. Then it is easy to see that after one pass with a median filter it will be reduced. This is demonstrated in figure 22. In the top frame, one of the

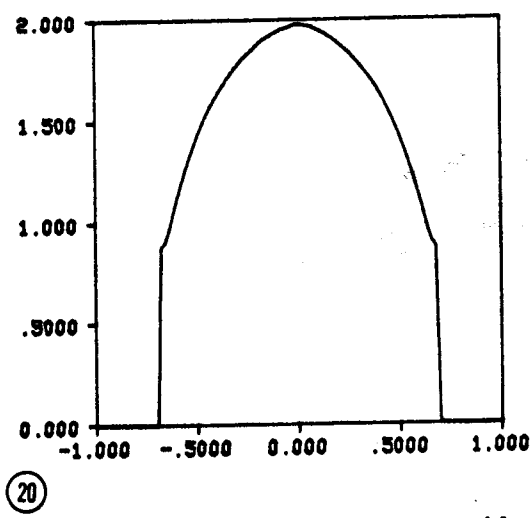

(20)

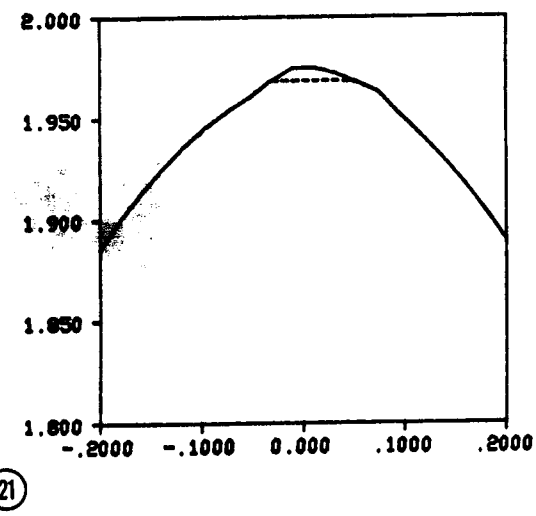

(21)

Fig. 20 Projection of the Shepp and Logan head phantom.

Fig. 21 Central portion of projection shown in figure 20. Dashed line is result after median filtering.

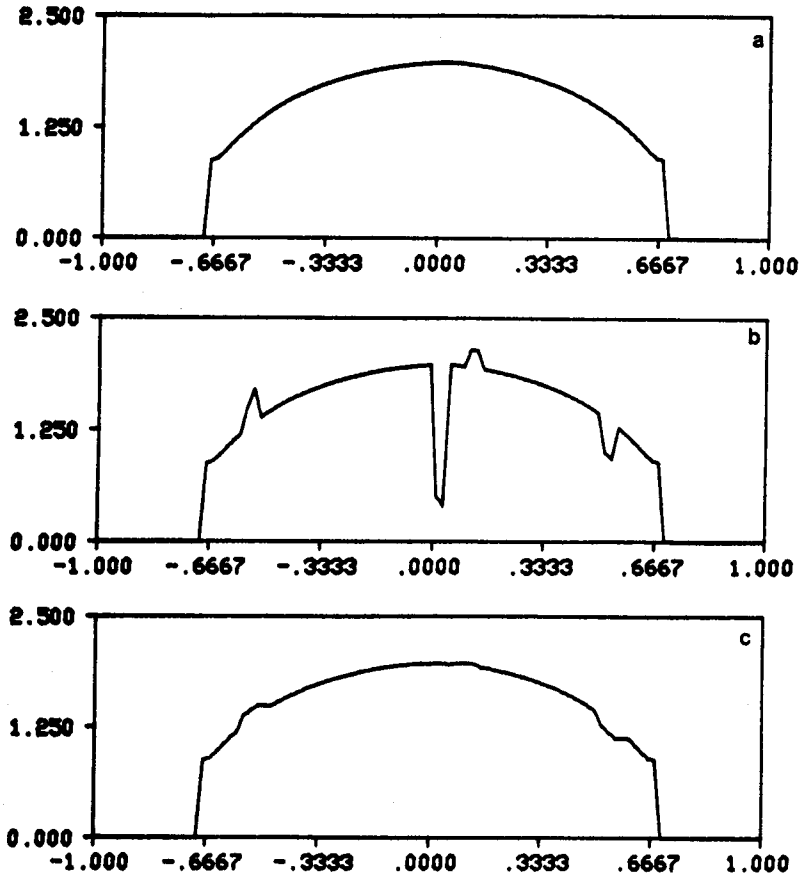

Fig. 22 (a) Projection of the Shepp and Logan head phantom. (b) Same as (a) but impulse noise has been added. (c) Result of (b) passed through a median filter.

projections of the Shepp and Logan head phantom is presented. In the middle frame glitch noise of length two samples has been added to the correct projection at different positions. The result after median filter of length J=2 is shown in the bottom frame. The glitch noise has been reduced.

Thus, it is seen that if multipath can be modeled by glitch noise in the projection space, then a median filter can be used to remove it. A demonstration of the ability of median filtering to reduce the artifacts caused by multipath is shown in the next section.

5. EXPERIMENTAL RESULTS

In this section the correction methods for multipath are evaluated. The correction methods are tested using data obtained from scanning two tissue equivalent phantoms. These phantoms are used instead of biological samples because they allow for a more quantitative evaluation of the resulting tomograms. A description of the scanner used to collect the data can be be found elsewhere [38].

23

Fig. 23 ATS Laboratories phantom.

Fig. 24 Time-of-flight reconstruction of the ATS phantom.

All of the reconstructions shown in this section are obtained with a fixed set of parameters. Each tomogram is reconstructed using 50 projections. Each projection is sampled at 100 locations. The images are displayed on a 128 by 128 display raster.

The attenuation images are obtained with the frequency shift method. The normalized first moment is used to calculate the center frequency of the power spectra. A 256 point Fast Fourier Transform is used to calculate power spectra. When homomorphic filtering is applied, only three samples are retained per cepstrum. In the case of a median filter, a window with length J=2 is used.

The first phantom used to test the multipath correction methods was constructed by the ATS Laboratories in Norwalk, CT. A picture of this phantom is shown in figure 23. The phantom was specifically designed to introduce multipath errors. The phantom is a piece of tissue equivalent oil gel [39]. The three holes and the quarter circle are filled with water.

Figure 24 shows a time-of-flight reconstruction of the ATS phantom. Figure 25(a) shows an attenuation image. There has been no compensation for multipath in this image. The two large streaks in figure 25(a) are due to artifacts introduced by the scanner. When one compares the time-of-flight and the attenuation tomograms, it is clear that the former tomogram is a better image.

Homomorphic filtering, as a correction method, is now applied to the received waveforms. The resulting attenuation image is shown in figure 25(b). The reconstruction after median filtering the projections is shown in figure 25(c). Figure 25(d) shows the reconstruction when both homomorphic and median filters are simultaneously applied.

The images shown in figure 25 demonstrate how the correction methods improve the contrast of the reconstructions. The best image is probably the one

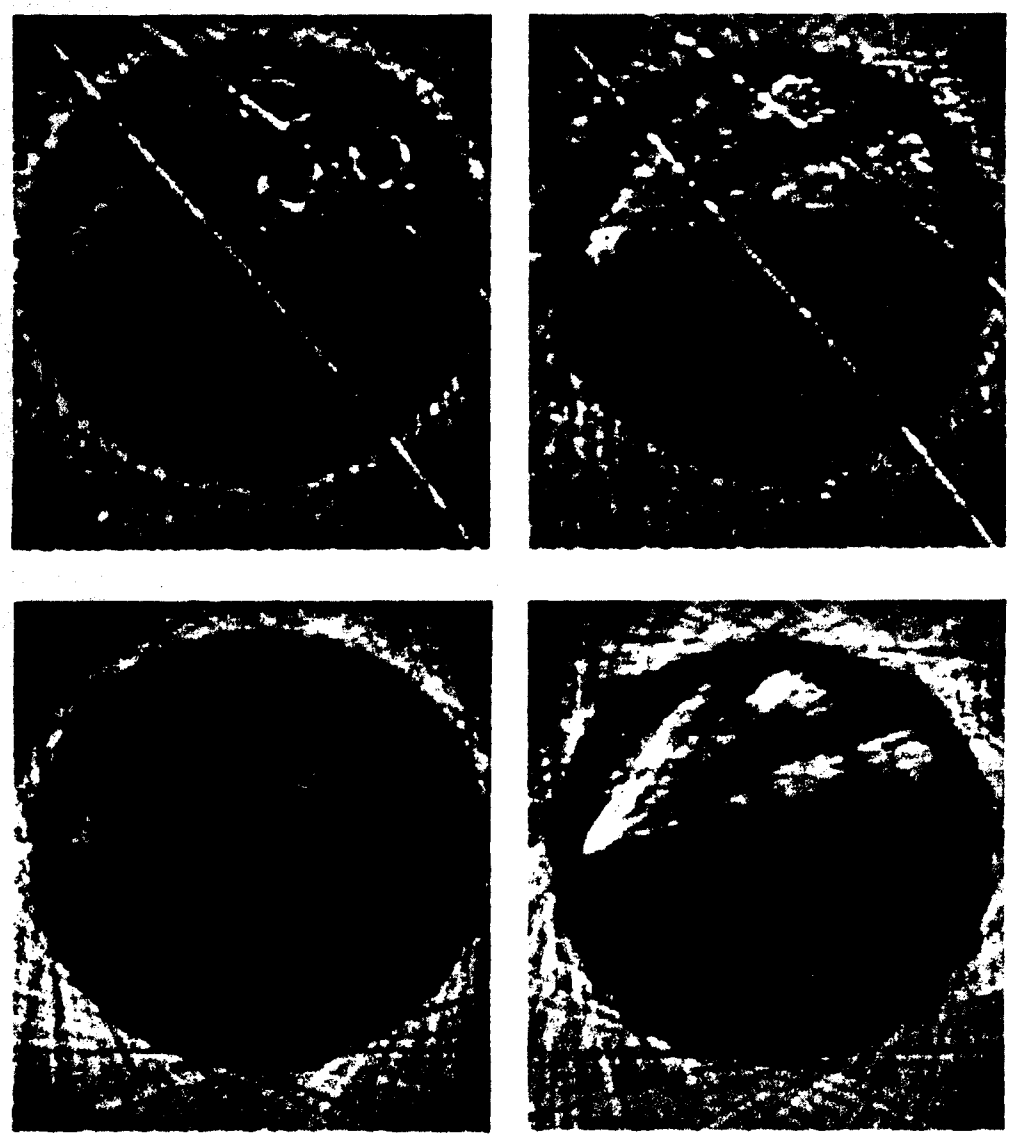

Fig. 25 Attenuation reconstruction of the ATS phantom. (a) Uncorrected. (b) Multipath compensation by homomorphic filtering. (c) Multipath compensation by median filtering. (d) Multipath compensation by homomorphic and median filtering.

where only median filtering is applied, figure 25(c). The image with the best contrast is the one where both homomorphic and median filters are applied, figure 25(d). It is obvious that improving the contrast also enhanced the artifacts due to refraction.

When one compares the time-of-flight reconstruction shown in figure 24 to the corrected attenuation image shown in figure 25(c), one sees that the two images are of similar quality. This implies that the errors in the attenuation estimates caused by the scalloped power spectra have been reduced.

Fig. 26 University of Wisconsin Breast phantom.

The second phantom used to test the multipath corrections is a breast phantom designed and built at the University of Wisconsin [40]. A picture of this phantom is shown in figure 26. At a level 2.5 cm below the base of the phantom are two simulated lipomas and two simulated tumors. The ultrasonic characteristics of the components of the phantom at this level are depicted in figure 27. An X-ray CT image of this plane is shown in figure 28. It should be noted that the ultrasound characteristics are not necessarily correlated with the x-ray characteristics. When comparing the x-ray images to the ultrasound images, only a geometrical comparison is valid.

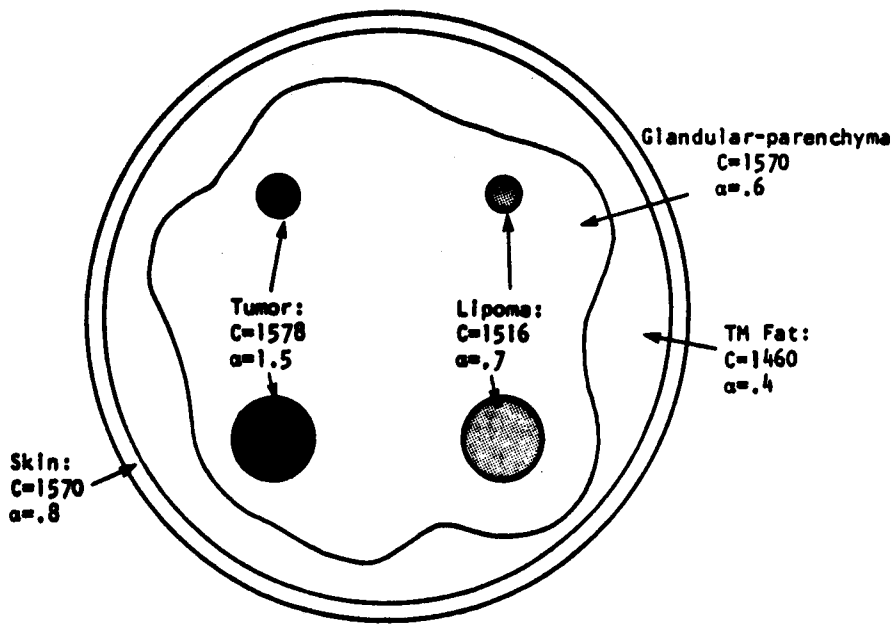

Fig. 27 Plane of the Breast 2.5 cm above the base of the phantom.

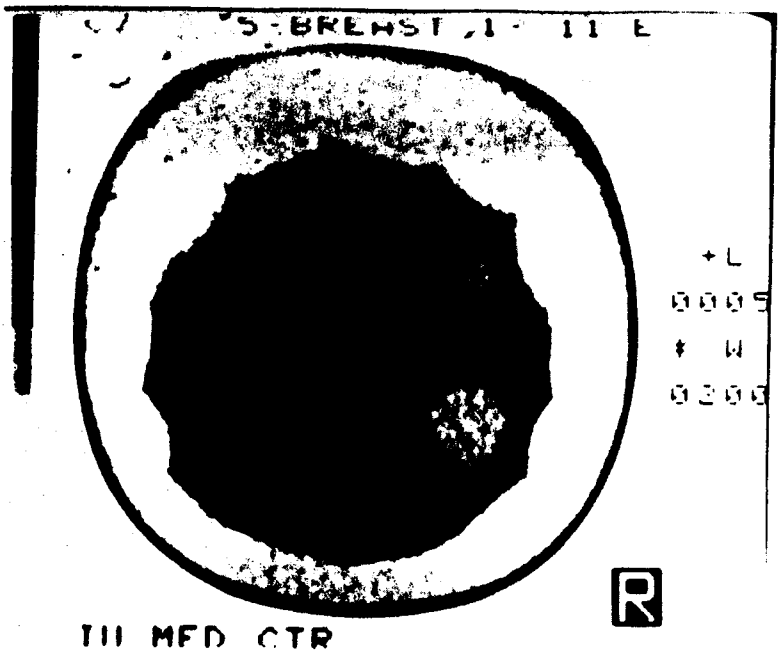

Fig. 28 X-ray CT image of the plane shown in figure 27.

A time-of-flight reconstruction of the plane containing the lipomas and tumors is shown in figure 29. The velocity of sound within the tumors, lipomas, glandular parenchyma, and the TM fat was measured to be 1556 m/s, 1506 m/s, 1551 m/s, and 1455 m/s, respectively. Thus, the imaging system produces images that are quantitatively correct to a high degree.

The uncorrected attenuation image is shown in figure 30(a). The results with homomorphic, median, and homomorphic and median filtering are also shown in figure 30. It is clear that the correction methods improve the quality of the

Fig. 29 Time-of-flight reconstruction of the breast phantom.

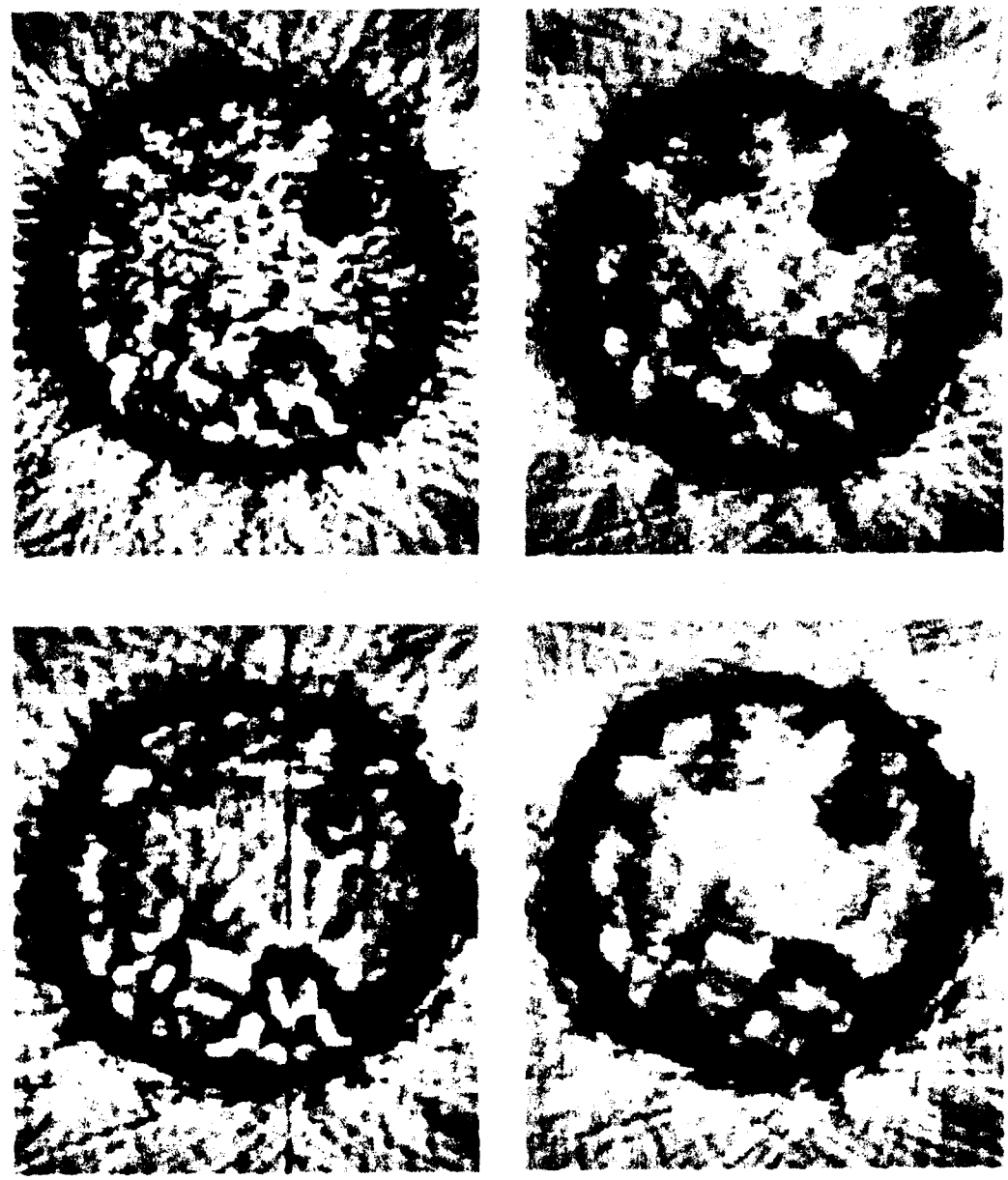

Fig. 30 Attenuation reconstruction of the breast phantom. (a) Uncorrected. (b) Multipath compensation by homomorphic filtering. (c) Multipath compensation by median filtering. (d) Multipath compensation by homomorphic and median filtering.

attenuation images. This is especially clear when one notices that the edge enhancements around the tumors and around the lipomas have been reduced. The edge artifact around the edge of the phantom was not completely eliminated because the assumptions used to justify the use of homomorphic and median filters break down when rays travel near edges. By break-down we mean that in the case of homomorphic filtering the relative arrival times are too small to be resolved; in the case of median filters the multipath error becomes systematic.

Direct conclusions cannot be made when the time-of-flight tomogram shown in figure 29 is compared to the corrected attenuation image shown in figure 30(d). This is because the attenuation coefficients of the components in the breast phantom are not linearly related to the respective velocity components. The two reconstructions are similar in the sense that the two tumors and two lipomas are visible in both sets of images and that they are of comparable size.

6. CONCLUSIONS

This report dealt with computed imaging techniques for ultrasonic tomography. Investigations included the development of estimation methods for integrated acoustic characteristics, artifact formation in ultrasonic tomograms, and correction procedures for multipath errors in images of the attenuation coefficient.

In Section 2 we concentrated on measurement techniques for estimating the refractive index and the attenuation coefficient. Initially we presented the time-of-flight methods for estimating the refractive index. Then, time-walk and time-hop artifacts in time-of-flight measurements were discussed. An estimator for the attenuation coefficient was also presented in Section 2.

In Section 2 we concentrated on estimating the acoustic parameters along the line-of-sight path between a transducer pair. In a tomographic application, it is possible for multiple rays to link the transducers. The existence of multipath along with curved ray paths, caused by refraction, invalidates the requirements for the reconstruction algorithm. This will result in artifacts in the reconstructed images.

In Section 3 we studied the artifacts generated when multipath is present in the received waveforms. We showed that multipath has a more adverse affect on estimates of the attenuation coefficient than on estimates of the refractive index.

Methods to correct for the artifacts caused by multipath were presented in Section 4. The first method, homomorphic filtering, tries to remove the scalloping in the power spectra caused by multipath. The second correction method, an application of median filtering, removes the inconsistencies in the projection domain that are caused by multipath.

In Section 5 the correction procedures were tested on data obtained by scanning two tissue equivalent phantoms. Results indicated that the methods significantly reduced the artifacts caused by multipath. Homomorphic and median filtering were equally successful in removing the multipath artifacts. Because of the added time needed to perform the additional Fourier transforms in homomorphic filtering, median filtering seems to be a more viable correction technique.

REFERENCES

[1] Housfield, G. N., "Computerized transverse axial scanning (tomography): part I. description of system," *British J. Radiology 46*, 1016-1022 (1973).

[2] Cope, O., *The Breast: Its Problems- Benign and Malignant- and How to Deal with Them* (Houghton Mifflin, Boston, 1977).

[3] Greenleaf, J. F., Johnson, S. A., Lee, S. L., Herman, G. T., and Wood, E. H., "Algebraic Reconstruction of Spatial Distributions of Acoustic Absorption within Tissue from their Two Dimensional Acoustic Projections," in *Acoustical Holography*, vol. 5, pp. 591-603 (Plenum Press, New York, 1974).

[4] Kak, A. C. and Dines, K. A., "Signal processing of broadband pulsed ultrasound: measurement of attenuation of soft biological tissues," *IEEE Trans. Biomed. Eng. BME-25*, 321-344 (1978).

[5] Dines, K. A. and Kak, A. C., "Ultrasonic attenuation tomography of soft biological tissues," *Ultrasonic Imaging 1*, 16-33 (1979).

[6] Klepper, J. R., Brandenburger, G. H., Busse, L. J., and Miller, J. G., "Phase Cancellation, Reflection, and Refraction Effects in Quantitative Ultrasonic Attenuation Tomography," in *1977 IEEE Ultrasonic Symp. Proc., pp. 182-188 (IEEE Cat. No. 77 CH 1264-1SU).*

[7] Greenleaf, J. F., Johnson, S. A., Samoya, W. F., and Duck, F. A., "Algebraic Reconstruction of Spatial Distributions of Acoustic Velocities in Tissue from their Time-of-flight Profiles," in *Acoustical Holography*, vol. 6, pp. 71-90 (Plenum Press, New York, 1975).

[8] Carson, P. L., Oughton, T. V., and Hendee, W. R., "Ultrasound Transaxial Tomography by Reconstruction," in *Ultrasound in Medicine*, vol. 2, White, D. N. and Barnes, R. W., eds., pp. 391-400 (Plenum Press, New York, 1976).

[9] Jakowatz, Jr., C. V. and Kak, A. C., "Computerized Tomography with X-rays and Ultrasound.", School of Elec. Eng., Purdue Univ., West Lafayette, IN, Res. Rep. TR-EE 76-26 (1976).

[10] Glover, G. H. and Sharp, J. L., "Reconstruction of ultrasound propagation speed distribution in soft tissue: time-of-flight tomography,", *IEEE Trans. Sonics Ultrasonics 24*, 229-234 (1977).

[11] Dines, K. A. and Kak, A. C., "Measurement and Reconstruction of Ultrasonic Parameters for Diagnostic Imaging," School of Elec. Eng., Purdue Univ., West Lafayette, IN, Res. Rep. TR-EE 77-4 (1976).

[12] Lizzi, F. L. and Coleman, D. J., "Ultrasonic Spectrum Analysis in Ophthalmalogy," in *Recent Advances in Ultrasound in Biomedicine*, vol. 1, White, D. N., ed., pp. 117-129 (Research Studies Press, Forest Grove, OR, 1977).

[13] Kuc, R., Schwartz, M., and Von Micsky, L., "Parametric Estimation of the Acoustic Attenuation Coefficient Slope for Soft Tissue," in *1976 IEEE Ultrasonics Symp. Proc.*, pp. 44-47 (IEEE Cat. No. 76 CH 1120-5SU).

[14] Oppenheim, A. V. and Schafer, R. W., *Digital Signal Processing*, ch. 10 (Prentice-Hall, Englewood Cliffs, NJ, 1975).

[15] Tukey, J. W., *Exploratory Data Analysis*, pp. 210-213 (Addison-Wesley, Reading, MA, 1977).

[16] Rosenfeld, A. and Kak, A.C., *Digital Picture Processing - 2nd Ed.*, Vol. 1, ch. 8 (Academic Press, New York, 1982).

[17] Wells, P. N. T., *Biomedical Ultrasonics* (Academic Press, London, 1977).

[18] Goldman, D. E. and Hueter, T. F., "Tabular data of the velocity and the absorption of high frequency sound in mammalian tissue," *J. Acoust. Soc. Amer. 28*, 35-37 (1956).

[19] Nicholas, D., "Orientation and Frequency Dependence of Backscattered Energy and its Clinical Application," in *Recent Advances in Ultrasound in Biomedicine*, vol. 1, White, D. N., ed., pp. 29-54 (Research Studies Press, Forest Grove, OR, 1977).

[20] Le Croissette, D. H., Heyser, R. C., Gammell, P. M., and Roseboro, J. A., "The Attenuation of Selected Soft Tissue as a Function of Frequency," in *Ultrasonic Tissue Characterization II*, Linzer, M., ed., National Bureau of Standards Spec. Publ. 525., pp. 101-108 (U. S. Government Printing Office, Washington, DC, 1979).

[21] Chivers, R. C. and Parry, R. J., "Ultrasonic velocity and attenuation in mammalian tissues," *J. Acoust. Soc. Amer. 63*, 940-953 (1978).

[22] Van Trees, H. L., *Detection, Estimation, and Modulation Theory, Part I* (Wiley, New York, 1968).

[23] Carson, P. L., Oughton, T. V., and Hendee, W. R., "Ultrasound Transaxial Tomography by Reconstruction," in *Ultrasound in Medicine*, vol. 2, White, D. N. and Barnes, R. W., eds., pp. 391-400 (Plenum Press, New York, 1976).

[24] Papoulis, A., *Probability, Random Variables, and Stochastic Processes*, p. 159 (McGraw-Hill, New York, 1965).

[25] Skolnik, M. I., *Introduction to Radar Systems - 2nd Ed.*, ch. 13 (McGraw Hill, New York, 1980).

[26] Robinson, D. E., "Computer Spectral Analysis of Ultrasonic A Mode Echoes," in *Ultrasonic Tissue Characterization II*, Linzer, M., ed., National Bureau of Standards Spec. Publ. 525., pp. 281-286 (U. S. Government Printing Office, Washington, DC, 1979).

[27] Wood, L. C. and Treitel, S., "Seismic signal processing", *Proc. IEEE 63*, 649-661 (1975).

[28] Fraser, J., Kino, G. S., and Birnholz, J., "Cepstral Signal Processing for Tissue Signal Analysis", in *Ultrasonic Tissue Characterization II*, Linzer, M., ed., National Bureau of Standards Spec. Publ. 525., pp. 287-295 (U. S. Government Printing Office, Washington, DC, 1979).

[29] Fjell, P. O., "Use of the cepstrum method for arrival times extraction of overlapping signals due to multipath conditions in shallow water," *J. Acoust. Soc. Amer. 59*, 209-211 (1976).

[30] Childers, D. G., Skinner, D. P., and Kemerait, R. C., "The cepstrum: a guide to processing," *Proc. IEEE 65*, 1428-1443 (1977).

[31] Hassab, J. C. and Boucher, R., "A probabilistic analysis of time delay extraction by the cepstrum in stationary Gaussian noise," *IEEE Trans. Inform. Theory IT-22*, 444-454, (1976).

[32] Gradshteyn, I. S., and Ryzhik, I. W., *Table of Integrals, Series, and Products* (Academic Press, New York, 1965).

[33] Yang, G. J. and Huang, T. S., "Median Filters and their Applications to Image Processing," School of Elec. Eng., Purdue Univ., West Lafayette, IN, Res. Rep TR-EE 80-1 (1980).

[34] Justusson, B., "Noise Reduction by Median Filtering," in *Proc. IEEE Conf. on Image Processing*, pp. 502-504 (IEEE Press, New York, 1978).

[35] Rabiner, L. R., Sambur, M. R., and Schmidt, C. E., "Applications of a nonlinear smoothing algorithm to speech processing," *IEEE Trans. Acoustics, Speech, Signal Processing ASSP-23*, 552-557 (1975).

[36] Gallagher, Jr., N. C., and Wise, G. L., "A theoretical analysis of the properties of median filters," *IEEE Trans. Acoustics, Speech, Signal Processing ASSP-29*, 1136-1141 (1981).

[37] Shepp, L. A. and Logan, B. F., "The Fourier reconstruction of a head section," *IEEE Trans. Nucl. Sci. NS-21*, 21-43 (1974).

[38] Crawford, C. R. and Kak, A. C., "Multipath Artifacts in Ultrasonic Transmission Tomography," School of Elec. Eng., Purdue Univ., West Lafayette, IN, Res. Rep. TR-EE 81-43 (1981).

[39] Scherzingen, A. L., Carson, P. L., Carter, W., Clayman, W., Johnson, M. L., Rashbaum, C., and Smith, S., "A Tissue Equivalent Upper Abdominal Phantom for Training and Equipment Demonstration," *Proc. AIUM*, paper 1734, Annual Meeting (American Institute for Ultrasound in Medicine, Bethesda, MD, 1979), Abstract only.

[40] Madsen, E. L., Zagzebski, J., Frank, G., Greenleaf, J. F., and Carson, P. L., "Anthropomorphic breast phantoms for assessing ultrasonic imaging system performance and for training ultrasonographers," *J. Clinical Ultrasound* (in press).